Supplement of Atmos. Chem. Phys., 20, 13011–13022, 2020
https://doi.org/10.5194/acp-20-13011-2020-supplement

Atmospheric Chemistry and Physics
Open Access
EGU

Supplement of

On the role of trend and variability in the hydroxyl radical (OH) in the global methane budget

Yuanhong Zhao et al.

Correspondence to: Yuanhong Zhao (yuanhong.zhao@lsce.ipsl.fr) and Bo Zheng (bo.zheng@lsce.ipsl.fr)

S1 Estimation of OH production and loss processes

The OH productions including $O(^1D)+H_2O$, $NO+HO_2$, and O_3+HO_2, and OH loss by CO (excluding EMAC) are provided as direct CCMI output listed in the Table S1. OH losses including the reactions with CO (only for EMAC), CH_4, isoprene, and CH_2O, which cannot be directly accessed from CCMI output, are approximately calculated by post-processing the CCMI output of the mixing ratios of reactive species, air pressure, temperature, and reaction coefficients from literature. The reaction coefficients for CESM and EMAC model are from Emmons et al. (2010) and Jöckel et al. (2016), respectively, as listed in table S1. For MRI-ESM1r1 and GEOSCCM, we use the same reaction coefficients with CESM. By comparing the reaction coefficients used in the CESM and EMAC at 273K and 288K, (table S1), one can see those reaction coefficients from different studies show small differences, which are less than 1% for the reaction of CH_4+OH, 2% for isoprene+OH, and 6% for CH_2O+OH. The comparisons show that using the same reaction coefficient for different models results in small uncertainties in the estimates of OH loss processes.

Table S1. Estimation of OH productions and losses.

By CCMI output	**Production**	**CCMI variable**	**description**	
	$O(^1D)+H_2O$	losso1dviah2o	Loss rate of $O(^1D)$ via $O(^1D)$+H2O	
	$NO+HO_2$	prodo3viaho2	Production Rate of O_3 via HO_2+NO	
	O_3+HO_2	losso3viaho2	Loss Rate of O_3 via O_3+HO_2	
	Loss	**CCMI variable**	**description**	
	CO+OH	lossco	Rate of CO Oxidation	
By reaction rates	**Loss**	**Reaction coefficient[a]**	**R_{273}[b]**	**R_{288}[c]**
	CO+OH(EMAC)	$1.57\times10^{-13}+3.54\times10^{-33}\times[M]$[d]	2.52×10^{-13}[e]	2.52×10^{-13}
	CH_4+OH(CESM)	$2.45\times10^{-12}\times EXP(-1775.\times1/Ta)$[f]	3.68×10^{-15}	5.16×10^{-15}
	CH_4+OH(EMAC)	$1.85\times10^{-20}Ta^{2.08}\times EXP(-987/Ta)$	3.69×10^{-15}	5.18×10^{-15}
	Isoprene+OH(CESM)	$3.1\times10^{-11}\times EXP(350/Ta)$	1.12×10^{-10}	1.04×10^{-10}
	Isoprene+OH(EMAC)	$2.54\times10^{-11}\times EXP(410/Ta)$	1.14×10^{-12}	1.05×10^{-10}
	CH_2O+OH(CESM)	9×10^{-12}	9×10^{-12}	9×10^{-12}
	CH_2O+OH(EMAC)	$9.52\times10^{-18}\times Ta^{2.03}\times EXP(636/ta)$	8.63×10^{-12}	8.51×10^{-12}

[a] The reaction coefficients are in the unit of cm^{-3} $molec^{-1}$ s^{-1}

[b] R_{273} is the chemical reaction coefficient at 273K

[c] R_{288} is the chemical reaction coefficient at 288K

[d] [M] is the concentration of air molecules in the unit of molec cm^{-3}.

[e] The R273 and R288 for CO+OH are calculated at sea surface pressure (1013.25hPa).
[f] Ta is the air temperature in the unit of K.

S2 Bayesian inversion

Both the two-box model inversions and the 3-D model inversions optimize CH_4 emissions through minimizing the cost function J, which is defined as:

$$J(\boldsymbol{x}) = \frac{1}{2}(\boldsymbol{x} - \boldsymbol{x^b})^T \mathbf{B}^{-1}\left(\boldsymbol{x} - \boldsymbol{x^b}\right) + \frac{1}{2}(H(\boldsymbol{x}) - \boldsymbol{y})^T \mathbf{R}^{-1}(H(\boldsymbol{x}) - \boldsymbol{y})$$

Here $\boldsymbol{x}$ is the state vector that includes initial conditions and CH_4 emissions. The CH_4 loss (mainly by reaction with OH) is prescribed and not optimized. $\boldsymbol{x^b}$ is the vector of prior emissions, here we use the emission in 2000 from the GCP inventory (Saunois et al., 2020). **B** is the prior error covariance matrix and **R** is the observation error covariance matrix. $H(\boldsymbol{x})$ is the projection from the state vector ($\boldsymbol{x}$) to the observational vector $\boldsymbol{y}$, which is either the two-box model or the 3-D LMDz model.

We set up the two-box model inversions following Turner et al. (2017). The inversions optimize hemispheric yearly emissions and initial conditions of CH_4 through assimilating mean CH_4 mixing ratios in each hemisphere generated from the Earth System Research Laboratory of the US National Oceanic and Atmospheric Administration (Dlugokencky, NOAA/ESRL, 2020). The two box-model can be approximated to a linear system since we do not optimize OH. We assume Gaussian errors and directly estimate the analytical solutions:

$$\boldsymbol{x} = \boldsymbol{x_b} + \boldsymbol{B}\boldsymbol{K}^T(\boldsymbol{K}\boldsymbol{S_A}\boldsymbol{K}^T + \boldsymbol{R})^{-1}(\boldsymbol{y} - H(\boldsymbol{x}))$$

Here K is the linear expression of $H(\boldsymbol{x})$.

The LMDz inversions optimize CH_4 emissions every 8 hours at the model resolution (3.75 ºongtitude ×1.85 ºatitude) and initial conditions at 20 °×15 °. The observational vector is also constructed by gathering surface observations from the NOAA/ESRL(Dlugokencky et al. 2020) network and assimilated by comparing with model-simulated CH_4 at the corresponding model grid-cell and time duration of the observations. The inversion system accesses the CH_4 emissions by iteratively

minimizing the cost function J with the M1QN3 algorithm (Gilbert and Lemaréchal, 1989).

S3 MEI

We use the bi-monthly Multivariate ENSO Index Version 2 (MEI, Wolter et al., 1998; 2001; Kobayashi et al., 2015; Zhang et al., 2019) to represent the ENSO strength. The MEI is estimated as the first principal component of the Empirical Orthogonal Function of the anomalies of 5 ENSO related variables over the tropical Pacific (30 °S-30 °N and 100 °E-70 °W). A positive MEI is corresponding to the El Niño event, while a negative MEI is corresponding to the La Niña event.

Table S2. Global and regional CH_4 losses by reaction with OH and CH_4 emissions estimated by variational inversions (Inv_OH_std and Inv_OH_cli) for the four periods.

CH_4 loss by OH (Tg yr^{-1})	1995-1996		1997-1998		97-98 minus 95-96	
	Inv_OH_std	Inv_OH_cli	Inv_OH_std	Inv_OH_cli	Inv_OH_std	Inv_OH_cli
90 °-30 °S	45	44	45	45	-0.5	0.1
30 °S-30 °N	353	348	345	350	-7	2
30 °-60 °N	70	69	69	69	-1	0.2
60 °-90 °N	8	8	8	8	-0.2	0.0
Global	475	470	466	471	-9	2
CH_4 loss by OH (Tg yr^{-1})	2001-2003		2007-2009		07-09 minus 01-03	
	Inv_OH_std	Inv_OH_cli	Inv_OH_std	Inv_OH_cli	Inv_OH_std	Inv_OH_cli
90 °-30 °S	45	45	46	45	0.7	0.3
30 °S-30 °N	356	353	366	356	10	3
30 °-60 °N	71	70	73	71	2	0.8
60 °-90 °N	8	8	8	8	0.3	0.1
Global	480	476	493	480	13	4
CH_4 emissions	1995-1996		1997-1998		97-98 minus 95-96	

(Tg yr^{-1})	Inv_OH_std	Inv_OH_cli	Inv_OH_std	Inv_OH_cli	Inv_OH_std	Inv_OH_cli
90 °-30 °S	16	16	16	16	0.0	0.2
30 °S-30 °N	275	271	278	280	3	10
30 °-60 °N	172	172	177	179	5	7
60 °-90 °N	25	26	26	26	0.8	0.8
Global	488	484	496	501	8	17
CH_4 emissions	2001-2003		2007-2009		07-09 minus 01-03	
(Tg yr^{-1})	Inv_OH_std	Inv_OH_cli	Inv_OH_std	Inv_OH_cli	Inv_OH_std	Inv_OH_cli
90 °-30 °S	15	15	15	14	-0.4	-0.7
30 °S-30 °N	277	274	293	281	16	7
30 °-60 °N	174	174	187	185	12	10
60 °-90 °N	24	24	26	26	2	2
Global	491	487	520	505	30	18

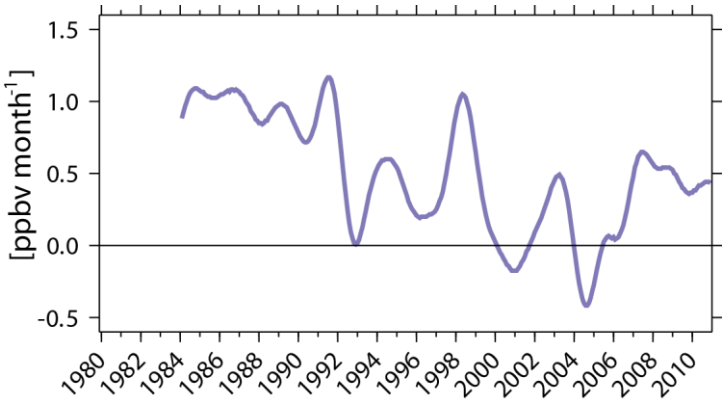

Figure S1. Global CH_4 growth rate computed from NOAA/ESRL observations (Dlugokencky, NOAA/ESRL, 2020).

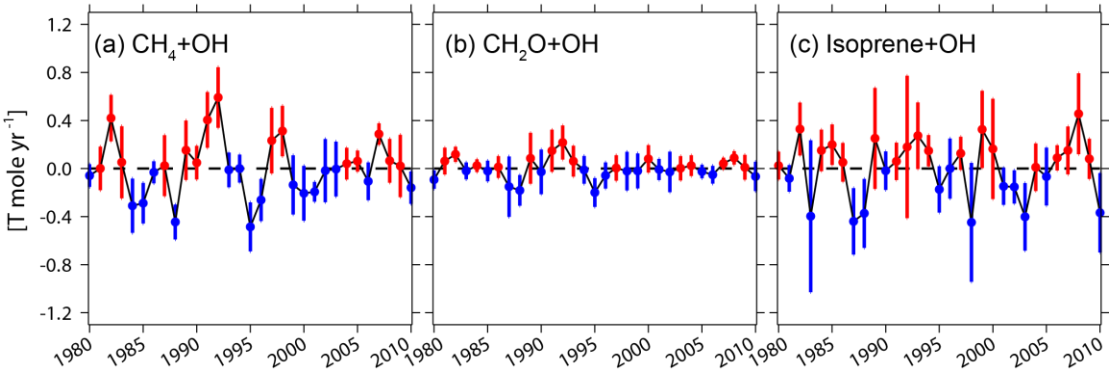

Figure S2. Anomaly of the detrended annual global total OH tendency from the reaction of CH_4+OH, CH_2O+OH, and isoprene+OH. The error bars are the one standard deviation of different models. Red and blue bars indicate positive and negative anomalies of multi-model mean values, respectively.

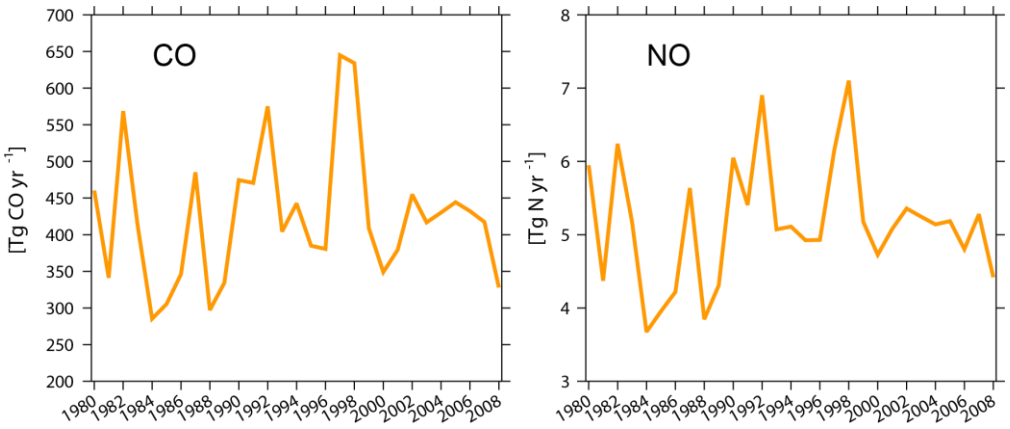

Figure S3. Global total biomass burning emissions for CO (left) and NO (right) from MACCity inventory (Granier et al., 2011) that used in CCMI model simulations.

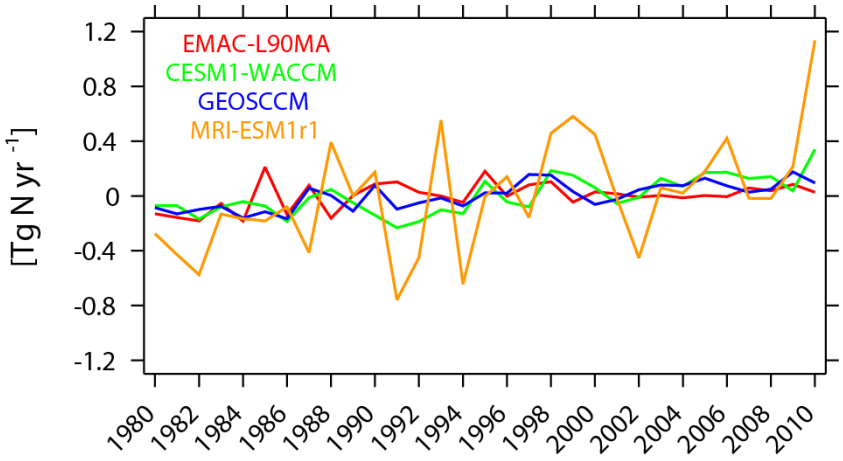

Figure S4. The anomalies in global total lightning nitrogen oxide emissions (NO, in [Tg N yr^{-1}]) estimated by CCMI models.

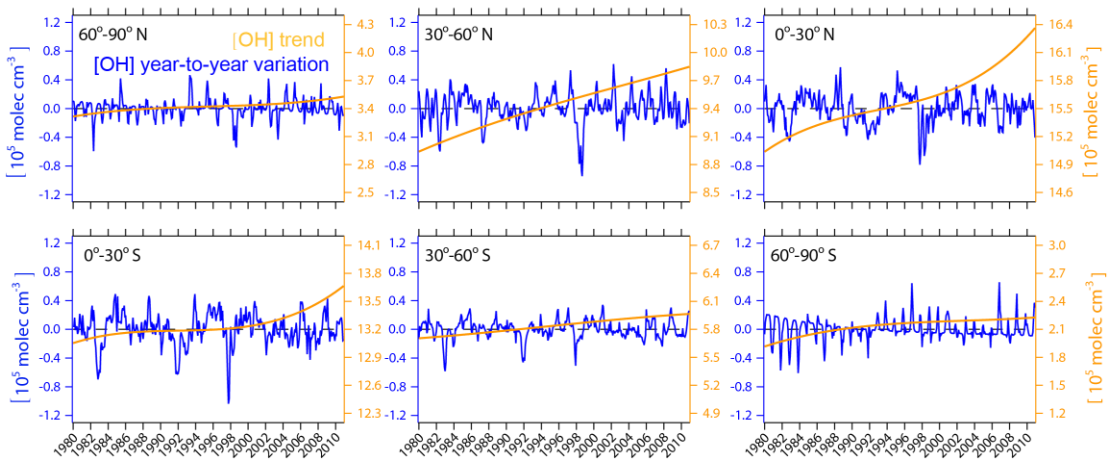

Figure S5. Anomaly of detrended and deseasonalized monthly mean tropospheric OH concentration ($[OH]_{GM\text{-}CH4}$, CH_4 reaction weighted, blue lines, corresponding to the left axis) and annual mean $[OH]_{GM\text{-}CH4}$ with year-to-year variations removed (yellow lines, right axis) averaged over six latitudinal intervals of the multi-model mean OH field.

References

Dlugokencky, NOAA/ESRL ,www.esrl.noaa.gov/gmd/ccgg/trends_ch4/ (last access: January 2020).

Emmons, L. K., Walters, S., Hess, P. G., Lamarque, J. F., Pfister, G. G., Fillmore, D., Granier, C., Guenther, A., Kinnison, D., Laepple, T., Orlando, J., Tie, X., Tyndall, G., Wiedinmyer, C., Baughcum, S. L., and Kloster, S.: Description and evaluation of the Model for Ozone and Related chemical Tracers, version 4 (MOZART-4), Geosci. Model Dev., 3, 43-67, 10.5194/gmd-3-43-2010, 2010.

Granier, C., Bessagnet, B., Bond, T., D'Angiola, A., Denier van der Gon, H., Frost, G. J., Heil, A., Kaiser, J. W., Kinne, S., Klimont, Z., Kloster, S., Lamarque, J.-F., Liousse, C., Masui, T., Meleux, F., Mieville, A., Ohara, T., Raut, J.-C., Riahi, K., Schultz, M. G., Smith, S. J., Thompson, A., van Aardenne, J., van der Werf, G. R., and van Vuuren, D. P.: Evolution of anthropogenic and biomass burning emissions of air pollutants at global and regional scales during the 1980–2010 period, Climatic Change, 109, 163, https://doi.org/10.1007/s10584-011-0154-1, 2011.

Gilbert, J. C., and Lemaréchal, C.: Some numerical experiments with variable-storage quasi-Newton algorithms, Mathematical programming, 45, 407-435, 1989.

Granier, C., Bessagnet, B., Bond, T., D'Angiola, A., Denier van der Gon, H., Frost, G. J., Heil, A., Kaiser, J. W., Kinne, S., Klimont, Z., Kloster, S., Lamarque, J.-F., Liousse, C., Masui, T., Meleux, F., Mieville, A., Ohara, T., Raut, J.-C., Riahi, K., Schultz, M. G., Smith, S. J., Thompson, A., van Aardenne, J., van der Werf, G. R., and van Vuuren, D. P.: Evolution of anthropogenic and biomass burning emissions of air pollutants at global and regional scales during the 1980–2010 period, Climatic Change, 109, 163, https://doi.org/10.1007/s10584-011-0154-1, 2011.

Jöckel, P., Tost, H., Pozzer, A., Kunze, M., Kirner, O., Brenninkmeijer, C. A. M.,

Brinkop, S., Cai, D. S., Dyroff, C., Eckstein, J., Frank, F., Garny, H., Gottschaldt, K.-D., Graf, P., Grewe, V., Kerkweg, A., Kern, B., Matthes, S., Mertens, M., Meul, S., Neumaier, M., Nützel, M., Oberländer-Hayn, S., Ruhnke, R., Runde, T., Sander, R., Scharffe, D., and Zahn, A.: Earth System Chemistry integrated Modelling (ESCiMo) with the Modular Earth Submodel System (MESSy) version 2.51, Geoscientific Model Development, 9, 1153-1200, 10.5194/gmd-9-1153-2016, 2016.

Kobayashi, S., Ota, Y., Harada, Y., Ebita, A., Moriya, M., Onoda, H., Onogi, K., Kamahori, H., Kobayashi, C., Endo, H., Miyaoka, K., and Takahashi, K.: The JRA-55 Reanalysis: General Specifications and Basic Characteristics, Journal of the Meteorological Society of Japan. Ser. II, 93, 5-48, 10.2151/jmsj.2015-001, 2015.

Saunois, M., Stavert, A. R., Poulter, B., Bousquet, P., Canadell, J. G., Jackson, R. B., Raymond, P. A., Dlugokencky, E. J., Houweling, S., Patra, P. K., Ciais, P., Arora, V. K., Bastviken, D., Bergamaschi, P., Blake, D. R., Brailsford, G., Bruhwiler, L., Carlson, K. M., Carrol, M., Castaldi, S., Chandra, N., Crevoisier, C., Crill, P. M., Covey, K., Curry, C. L., Etiope, G., Frankenberg, C., Gedney, N., Hegglin, M. I., Höglund-Isaksson, L., Hugelius, G., Ishizawa, M., Ito, A., Janssens-Maenhout, G., Jensen, K. M., Joos, F., Kleinen, T., Krummel, P. B., Langenfelds, R. L., Laruelle, G. G., Liu, L., Machida, T., Maksyutov, S., McDonald, K. C., McNorton, J., Miller, P. A., Melton, J. R., Morino, I., Müller, J., Murguia-Flores, F., Naik, V., Niwa, Y., Noce, S., O'Doherty, S., Parker, R. J., Peng, C., Peng, S., Peters, G. P., Prigent, C., Prinn, R., Ramonet, M., Regnier, P., Riley, W. J., Rosentreter, J. A., Segers, A., Simpson, I. J., Shi, H., Smith, S. J., Steele, L. P., Thornton, B. F., Tian, H., Tohjima, Y., Tubiello, F. N., Tsuruta, A., Viovy, N., Voulgarakis, A., Weber, T. S., van Weele, M., van der Werf, G. R., Weiss, R. F., Worthy, D., Wunch, D., Yin, Y., Yoshida, Y., Zhang, W., Zhang, Z., Zhao, Y., Zheng, B., Zhu, Q., Zhu, Q., and Zhuang, Q.: The Global Methane Budget 2000–2017, Earth Syst. Sci. Data, 12, 1561-1623, 10.5194/essd-12-1561-2020, 2020.

Turner, A. J., Frankenberg, C., Wennberg, P. O., and Jacob, D. J.: Ambiguity in the causes for decadal trends in atmospheric methane and hydroxyl, Proc Natl Acad Sci U S A, 114, 5367-5372, 10.1073/pnas.1616020114, 2017.

Wolter, K., and Timlin, M. S.: Measuring the strength of ENSO events: How does 1997/98 rank?, Weather, 53, 315-324, 10.1002/j.1477-8696.1998.tb06408.x, 1998.

Wolter, K., and Timlin, M. S.: El Niño/Southern Oscillation behaviour since 1871 as diagnosed in an extended multivariate ENSO index (MEI.ext), International Journal of Climatology, 31, 1074-1087, 10.1002/joc.2336, 2011.

Zhang, T., Hoell, A., Perlwitz, J., Eischeid, J., Murray, D., Hoerling, M., and Hamill, T. M.: Towards Probabilistic Multivariate ENSO Monitoring, Geophysical Research Letters, 46, 10532-10540, 10.1029/2019gl083946, 2019.